PNAS
www.pnas.org

Supplementary Information for

Default mode network streams for coupling to language and control systems

Evan M. Gordon, Timothy O. Laumann, Scott Marek, Ryan V. Raut, Caterina Gratton, Adrian W. Gilmore, Dillan J. Newbold, Deanna J. Greene, Rebecca S. Coalson, Abraham Z. Snyder, Bradley L. Schlaggar, Steven E. Petersen, Nico U.F. Dosenbach, Steven M. Nelson

Correspondence: Evan M. Gordon
Email: evan.gordon@va.gov

This PDF file includes:

Supplementary text
Figures S1 to S13
SI References

Other supplementary materials for this manuscript include the following:

None

www.pnas.org/cgi/doi/10.1073/pnas.2005238117

Supplementary Information Text

SUPPLEMENTAL METHODS

MRI image acquisition

Imaging for each subject was performed on a Siemens TRIO 3T MRI scanner over the course of 12 sessions conducted on separate days, each beginning at midnight. Structural MRI was conducted across two separate days. In total, four T1-weighted images (sagittal, 224 slices, 0.8 mm isotropic resolution, TE=3.74 ms, TR=2400 ms, TI=1000 ms, flip angle = 8 degrees), four T2-weighted images (sagittal, 224 slices, 0.8 mm isotropic resolution, TE=479 ms, TR=3200 ms), four MRA (transverse, 0.6 x 0.6, x 1.0mm, 44 slices, TR=25ms, TE=3.34ms) and eight MRVs, including four in coronal and four in sagittal orientations (sagittal: 0.8 x 0.8 x 2.0mm thickness, 120 slices, TR=27ms, TE=7.05ms; coronal: 0.7 x 0.7 x 2.5mm thickness, 128 slices, TR=28ms TE= 7.18ms), were obtained for each subject. Analyses of the MRA and MRV scans are not reported here.

On ten subsequent days, each subject underwent 1.5 hour functional MRI scanning beginning at midnight. In each session, we first collected thirty contiguous minutes of resting state fMRI data, in which subjects visually fixated on a white crosshair presented against a black background. Each subject was then scanned during performance of three separate tasks: motor (2 runs per session, 7.8 minutes combined), incidental memory (3 runs per session, 13.1 minutes combined), mixed design (2 runs per session, 14.2 minutes combined). Across all sessions, each subject was scanned for 300 total minutes during the resting state and approximately 350 total minutes during task performance. All functional imaging was performed using a gradient-echo EPI sequence (TR = 2.2 s, TE = 27 ms, flip angle = 90°, voxel size = 4 mm x 4 mm x 4 mm, 36 slices). In each session, one gradient echo field map sequence was acquired with the same prescription as the functional images. An EyeLink 1000 eye-tracking system (http://www.sr-research.com) allowed continuous monitoring of subjects' eyes in order to check for periods of prolonged eye closure, potentially indicating sleep. Only one subject (MSC08) demonstrated prolonged eye closures.

Task design

Motor task design: The motor task was adapted from that used in the Human Connectome Project (1). Subjects were presented with visual cues that directed them to close and relax their hands, flex and relax their toes, or wiggle their tongue. Each block started with a 2.2 s cue indicating which movement was to be made. After this cue, a centrally-presented caret replaced the instruction and flickered once every 1.1 s (without temporal jittering). Each time the caret flickered, subjects executed the proper movement. 12 movements were made per block. Each task run consisted of 2 blocks of each type of movement as well as 3 blocks of resting fixation, which lasted 15.4 s.

Incidental memory task: In this task, subjects made discrimination decisions about scenes, faces, and words, each of which was presented multiple times. Within each session, a single scan run was collected of each type of stimulus. In each task run, subjects viewed 24 stimuli, 3 times each. Stimuli were presented for 1.7 s with a jittered inter-stimulus interval ranging from 500-4900 ms. For scenes, subjects indicated whether an indoor or outdoor picture was presented. For faces, male/female judgments were made. For words, subjects made abstract/concrete judgments. Subjects were instructed to make their decisions as quickly as possible irrespective of the number of times a given stimulus had been presented. Subjects made their responses using a fiber-optic response box, and the finger used for each response type was counterbalanced within participants across sessions.

Mixed block/event-related design task: This task was adapted from experimental conditions reported by (2). One task was a spatial coherence discrimination task, which used concentric dot patterns (3) that were either 0% or 50% coherent. During this task, subjects had to identify each pattern as concentric or random. The other task was a verbal discrimination task. Subjects were presented with nouns and verbs, and had to identify which type of word was being presented on the screen. Task blocks began with a 2.2 s cue screen indicating which task was to be conducted in the following block. Blocks consisted of 30 trials (half concentric/half non-concentric for coherence, half noun/half verb for verbal). Stimuli were presented for 0.5 s with a variable 1.7-8.3 s ISI. A stop cue displayed for 2.2 s signaled the end of each task block. Each scan run consisted of two blocks of each task. Task blocks were separated by 44 s periods of rest. For each task, the finger used for each response was counterbalanced within participants across sessions. No words overlapped between this task and the implicit memory task.

Cortical surface generation

Generation of cortical surfaces from the MRI data followed a procedure similar to that previously described in (4). First, anatomical surfaces were generated from the subject's average T1-weighted image in native volumetric space using FreeSurfer's default recon-all processing pipeline (version 5.3). This pipeline first conducted brain extraction and segmentation. After this step, segmentations were hand-edited to maximize accuracy. Subsequently, the remainder of the recon-all pipeline was conducted on the hand-edited segmentations, including generation of white matter and pial surfaces, inflation of the surfaces to a sphere, and surface shape-based spherical registration of the subject's original surface to the fsaverage surface (5, 6). The fsaverage-registered left and right hemisphere surfaces were brought into register with each other using deformation maps from a landmark-based registration of left and right fsaverage surfaces to a hybrid left-right fsaverage surface ('fs_LR'; Van Essen et al., 2012). These fs_LR spherical template meshes were input to a flexible Multi-modal surface Matching (MSM) algorithm using sulc features to register templates to the atlas mesh (8). These newly registered surfaces were then down-sampled to a 32,492 vertex surface (fs_LR 32k) for each hemisphere. The various structural metric data (thickness, curvature, etc.) from the original surfaces to the fs_LR 32k surface were composed into a single deformation map allowing for one step resampling. MSM registration provided a more optimal fit of pial and white surfaces and reduced areal distortion (9). These various surfaces in native stereotaxic space were then transformed into atlas space (711-2B) by applying the previously calculated T1-to-atlas transformation.

fMRI Preprocessing

Functional data were preprocessed to reduce artifacts and to maximize cross-session registration. All sessions underwent correction of odd vs. even slice intensity differences attributable to interleaved acquisition, intensity normalization to a whole brain mode value of 1000, and within run correction for head movement. Atlas transformation was computed by registering the mean intensity image from a single BOLD session to Talairach atlas space (10) via the average high-resolution T2-weighted image and average high-resolution T1-weighted image. All subsequent BOLD sessions were linearly registered to this first session. This atlas transformation, mean field distortion correction (see below), and resampling to 3-mm isotropic atlas space were combined into a single interpolation using FSL's applywarp tool (11). All subsequent operations were performed on the atlas-transformed volumetric time series.

Distortion correction

A mean field map was generated based on the field maps collected in each subject (12). This mean field map was then linearly registered to each session and applied to that session for distortion correction. To generate the mean field map the following procedure was used: (1)

Field map magnitude images were mutually co-registered. (2) Transforms between all sessions were resolved. Transform resolution reconstructs the n-1 transforms between all images using the n(n-1)/2 computed transform pairs. (3) The resolved transforms were applied to generate a mean magnitude image. (4) The mean magnitude image was registered to an atlas representative template. (5) Individual session magnitude image to atlas space transforms were computed by composing the session-to-mean and mean-to-atlas transforms. (6) Phase images were then transformed to atlas space using the composed transforms, and a mean phase image in atlas space was computed.

Application of mean field map to individual fMRI sessions: (1) For each session, field map uncorrected data were registered to atlas space, as above. (2) The generated transformation matrix was then inverted and applied to the mean field map to bring the mean field map into the session space. (3) The mean field map was used to correct distortion in each native-space run of resting state and task data in the session. (4) The undistorted data were then re-registered to atlas space. (5) This new transformation matrix and the mean field map then were applied together to resample each run of resting state and task data in the session to undistorted atlas space in a single step.

RSFC Preprocessing

Additional preprocessing steps to reduce spurious variance unlikely to reflect neuronal activity were executed as recommended in (13, 14). First, temporal masks were created to flag motion-contaminated frames. We observed that two subjects (MSC 03 and MSC 10) had a high-frequency artifact in the motion estimates calculated in the phase encode (anterior-posterior) direction that did not appear to reflect biological movement. We thus filtered the motion estimate time courses in this direction only to retain effects occurring below 0.1 Hz in all subjects for consistency (15). Motion contaminated volumes were then identified by frame-by-frame displacement (FD). Frames with FD > 0.2mm were flagged as motion-contaminated. Across all subjects, these masks censored 28% ± 18% (range: 6% – 67%) of the data; on average, subjects retained 5929 ± 1508 volumes (range: 2733 – 7667), corresponding to 217 ± 55 minutes (range: 100 – 281).

After computing the temporal masks for high motion frame censoring, the data were processed with the following steps: (i) demeaning and detrending, (ii) linear interpolation across censored frames using so that continuous data can be passed through (iii) a band-pass filter (0.005 Hz < f < 0.01 Hz) without re-introducing nuisance signals (16) or contaminating frames near high motion frames (17).

Next, the filtered BOLD time series underwent a component-based nuisance regression approach (4). Nuisance regression using time series extracted from white matter and cerebrospinal fluid (CSF) assumes that variance in such regions is unlikely to reflect neural activity. Variance in these regions is known to correspond largely to physiological noise (e.g., CSF pulsations), arterial pCO2-dependent changes in T2*-weighted intensity and motion artifact; this spurious variance is widely shared with regions of interest in gray matter. We also included the mean signal averaged over the whole brain as a nuisance regressor. Global signal regression (GSR) has been controversial. However, the available evidence indicates that GSR is a highly effective de-noising strategy (13, 18).

Nuisance regressors were extracted from white matter and ventricle masks, first segmented by FreeSurfer (19), then spatially resampled in register with the fMRI data. Voxels surrounding the edge of the brain are particularly susceptible to motion artifacts and CSF pulsations (20, 21); hence, a third nuisance mask was created for the extra-axial compartment by thresholding the temporal standard deviation image (SDt > 2.5%), excluding a dilated whole brain mask. Voxel-wise nuisance time series were dimensionality reduced as in CompCor (22), except that the number of retained regressors, rather than being a fixed quantity, was determined, for each noise compartment, by orthogonalization of the covariance matrix and retaining components

ordered by decreasing eigenvalue up to a condition number of 30 (max eigenvalue / min eigenvalue > 30). The retained components across all compartments formed the columns of a design matrix, X, along with the global signal, its first derivative, and the six time series derived by retrospective motion correction. The columns of X are likely to exhibit substantial co-linearity. Therefore, to prevent numerical instability owing to rank-deficiency during nuisance regression, a second-level SVD was applied to XX^T to impose an upper limit of 250 on the condition number. This final set of regressors was applied in a single step to the filtered, interpolated BOLD time series, with censored data ignored during beta estimation. Finally, the data were upsampled to 2mm isotropic voxels. Censored frames were then excised from the data for all subsequent analyses.

Surface processing and CIFTI generation of BOLD data

Surface processing of BOLD data proceeded through the following steps. First, the BOLD fMRI volumetric timeseries (both resting-state and task) were sampled to each subject's original mid-thickness left and right-hemisphere surfaces (generated as the average of the white and pial surfaces) using the ribbon-constrained sampling procedure available in Connectome Workbench 1.0. This procedure samples data from voxels within the gray matter ribbon (i.e., between the white and pial surfaces) that lie in a cylinder orthogonal to the local mid-thickness surface weighted by the extent to which the voxel falls within the ribbon. Voxels with a timeseries coefficient of variation 0.5 standard deviations higher than the mean coefficient of variation of nearby voxels (within a 5 mm sigma Gaussian neighborhood) were excluded from the volume to surface sampling, as described in (23). Once sampled to the surface, timecourses were deformed and resampled from the individual's original surface to the 32k fs_LR surface in a single step using the deformation map generated above (in "Cortical surface generation"). This resampling allows point-to-point comparison between each individual registered to this surface space.

These surfaces were then combined with volumetric subcortical and cerebellar data into the CIFTI format using Connectome Workbench (24), creating full brain timecourses excluding non-gray matter tissue. Subcortical (including accumbens, amygdala, caudate, hippocampus, pallidum, putamen, and thalamus) and cerebellar voxels were selected based on the FreeSurfer segmentation of the individual subject's native-space average T1, transformed into atlas space, and manually inspected. Finally, the BOLD timecourses were smoothed with a geodesic 2D (for surface data) or Euclidean 3D (for volumetric data) Gaussian kernel of $\sigma = 2.55$ mm.

Task Analysis

Task evoked activations were modeled individually for each vertex and voxel with a general linear model (GLM) (25), using in-house image analysis software written in IDL (Research Systems, Inc.). First level GLM analyses were conducted separately for each session in a given subject, and second level within-subject analyses were run on the session-wise beta values of a single subject. Planned second-level contrasts were evaluated as paired voxel/vertex-wise t-tests comparing these beta values, and the resulting t-values in each voxel/vertex were then Z-transformed for further analysis.

The tasks had three different types of designs (motor = block design, coherence/semantic = mixed block/event-related design, incidental memory = event-related design). In the block design motor task, a block regressor was convolved with a canonical hemodynamic response to model the five experimental conditions: tongue, left hand, right hand, left foot, right foot. The contrast of interest in this work was (left hand + right hand) > tongue.

In the event-related incidental memory design, a finite impulse response (FIR) approach was used to model the timecourse of activations for each event, with a single delta function used to model each of 8 timepoints after a response; this approach has the advantage of making no assumptions regarding the shape of the hemodynamic response function (26).

Separate regressors were included for each stimulus type (male face, female face, indoor scene, outdoor scene, abstract word, concrete word) as well as the number of presentations of a given item (first, second, or third presentation). The contrast of interest in this work was (all scenes) > (all faces).

The coherence and semantic judgment tasks were jointly modeled in a mixed block-event-related design. Events were modeled with an FIR model (as above, with 8 timepoints for each event); separate event regressors were included for the start and end cues in each task, and for the different trial types (noun, verb, 50% coherence, 0% coherence). The block (sustained activity) was modeled with a square block regressor, with separate regressors for sustained activity in the semantic and coherence task. Given the low number of error trials, errors were not modeled in any task. In addition to these terms, constant and linear effects were modeled for each run. The contrast of interest in this work was the block effect of (semantic judgment) > (fixation).

Regression of adjacent cortical tissue from RSFC BOLD

Many subcortical areas, such as dorsal cerebellum and lateral putamen, are in close anatomical proximity to cortex, resulting in spurious functional coupling between the cortical vertices and adjacent subcortical voxels. To reduce this artifact, RSFC BOLD time series from all vertices falling within 20mm Euclidean distance of a source voxel were averaged and then regressed from the voxel time series (4, 27, 28). The resulting residual timeseries were used for all subsequent analyses.

SUPPLEMENTAL FIGURES

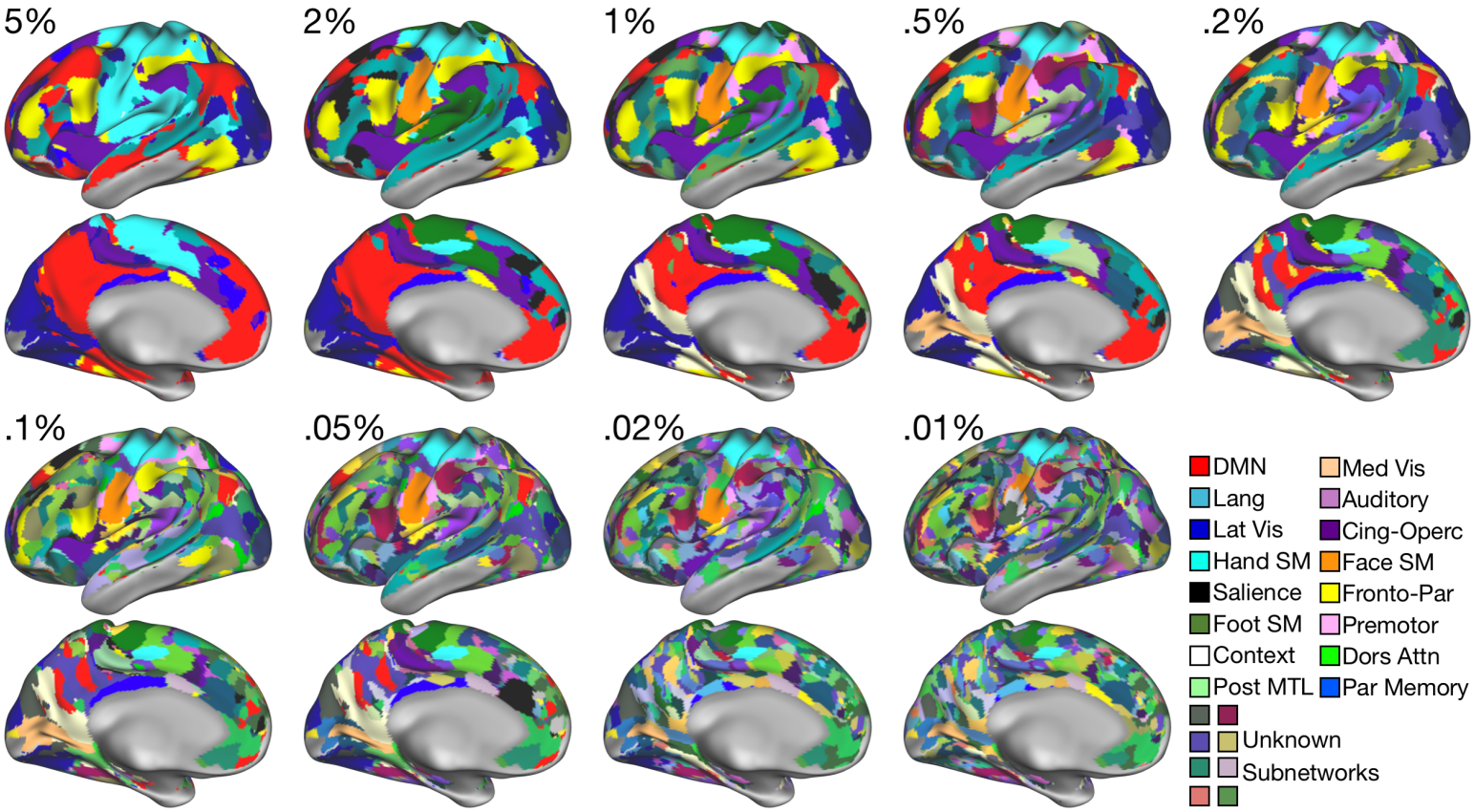

Figure S1: Brain networks at different density levels in example subject MSC01.

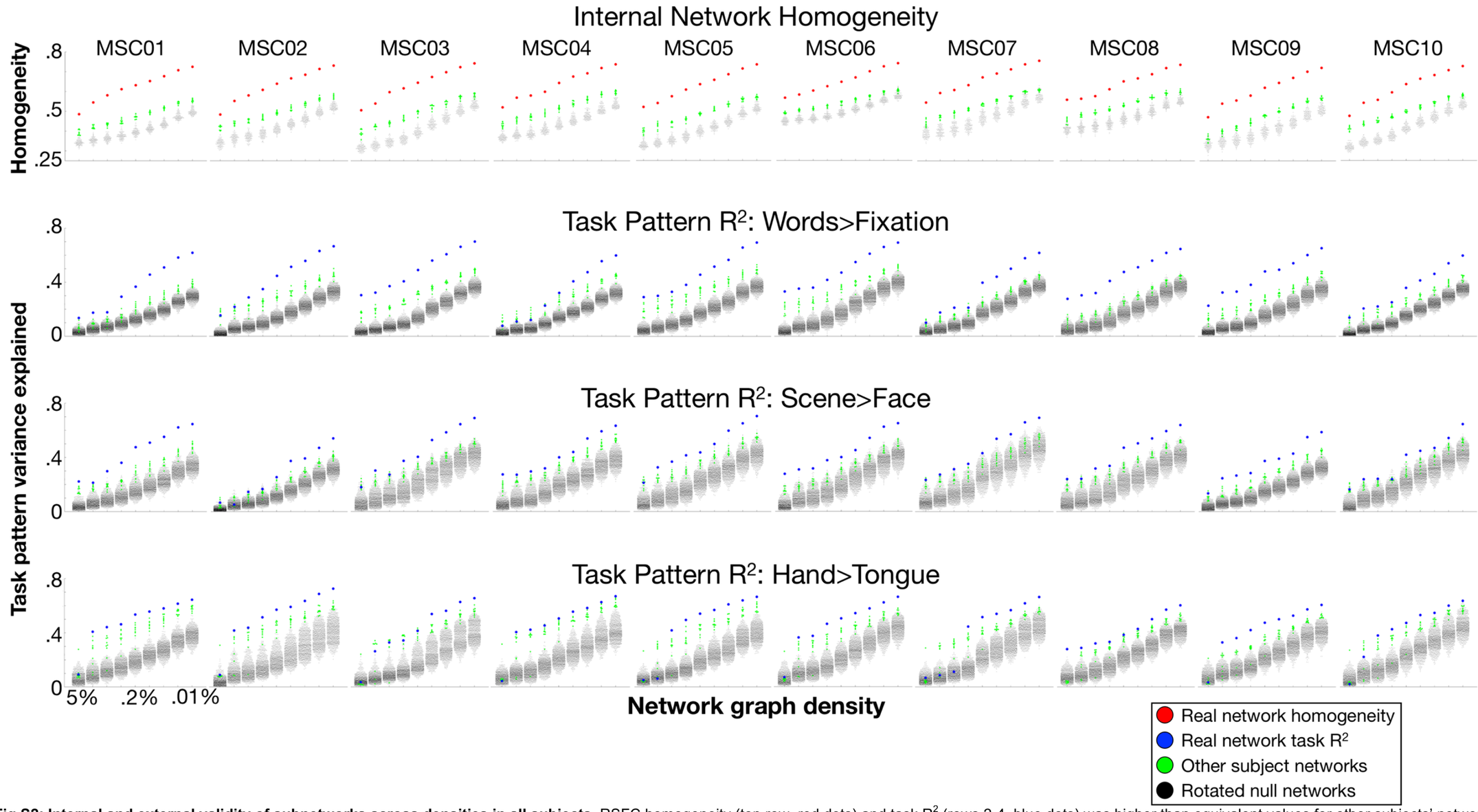

Fig S2: Internal and external validity of subnetworks across densities in all subjects. RSFC homogeneity (top row, red dots) and task R^2 (rows 2-4, blue dots) was higher than equivalent values for other subjects' networks (green dots) or rotated null networks (black dots), particularly at sparser thresholds (right side of each plot). Row 2: Words > Fixation contrast; row 3: Scene > Face contrast; Row 4: Hand > Tongue contrast.

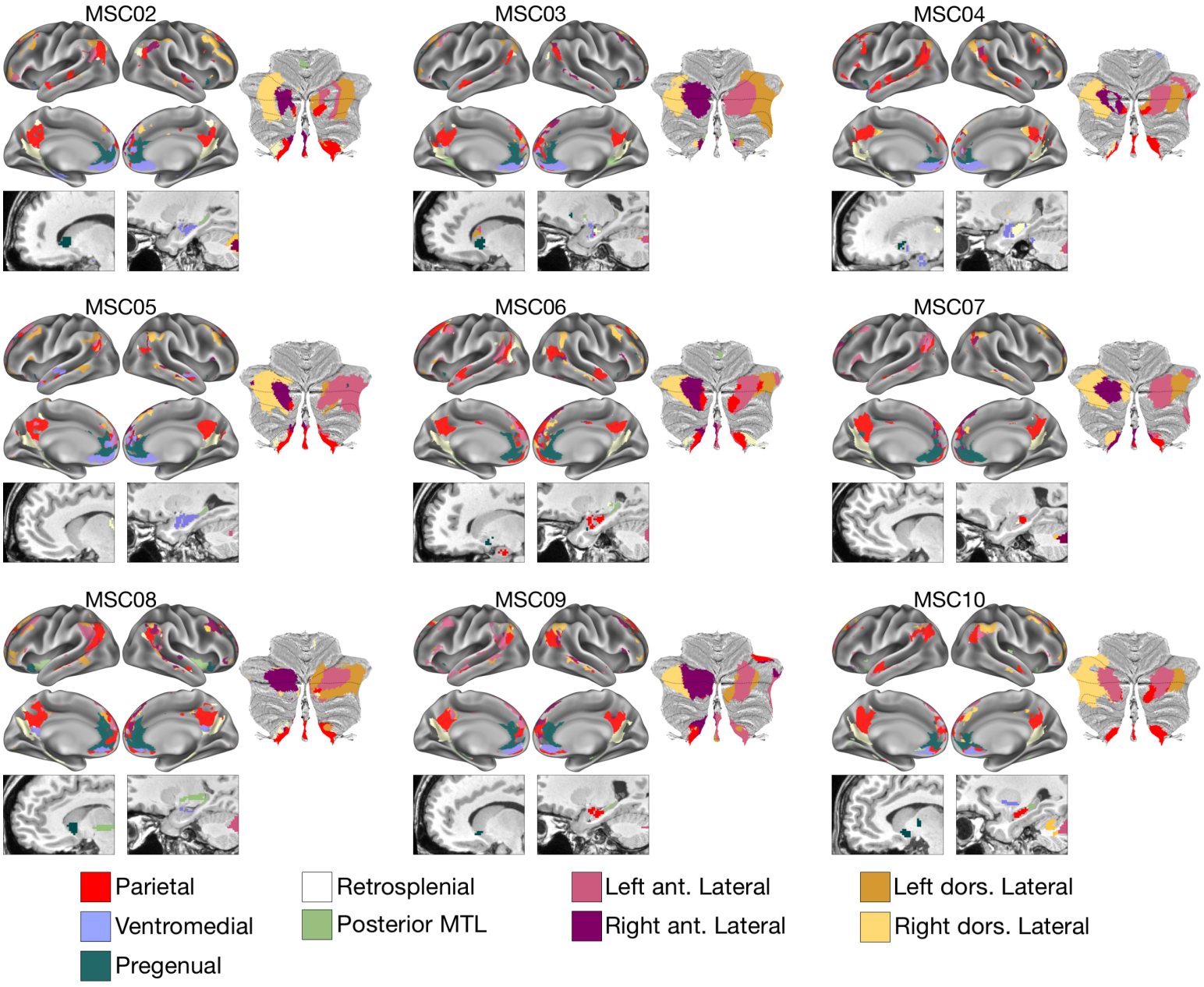

Figure S3: DMN subnetworks in subjects MSC02-10. For each subject, different colors represent different subnetworks in cortex (top left), ventral caudate and medial temporal lobe (bottom left), and cerebellum (right).

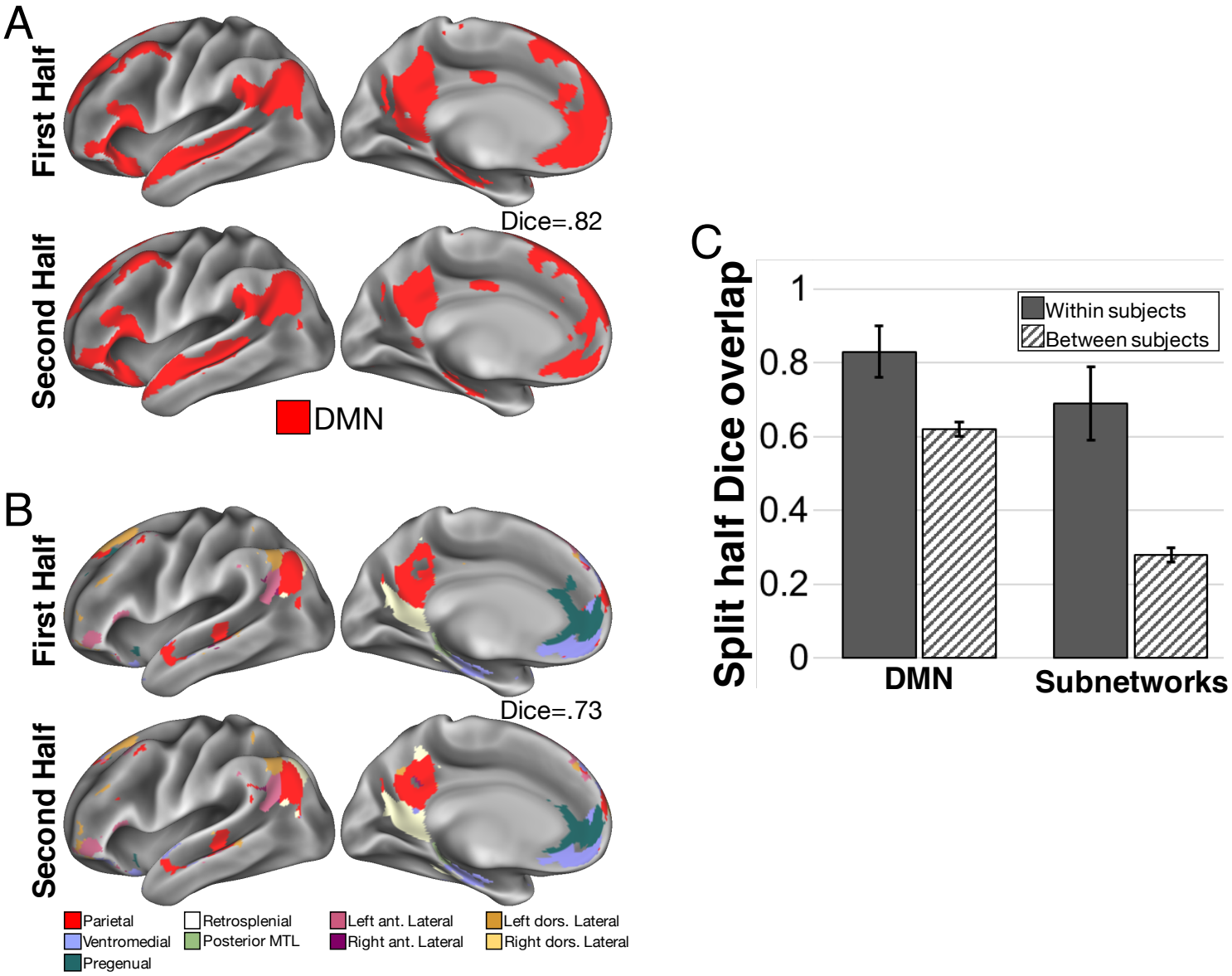

Figure S4: Reproducibility and individual identifiability of DMN networks and subnetworks. A,B) DMN networks (A) and subnetworks (B) identified in split halves of an example subject's data. C) Across subjects, both DMN networks (left) and subnetworks (right) delineated from split halves pf each subject's data were more similar within subjects (solid bars) than between subjects (striped bars). However, the within-between difference was larger for subnetworks than for whole large-scale networks in every subject (paired $t(9)=8.19$; $p<10^{-4}$).

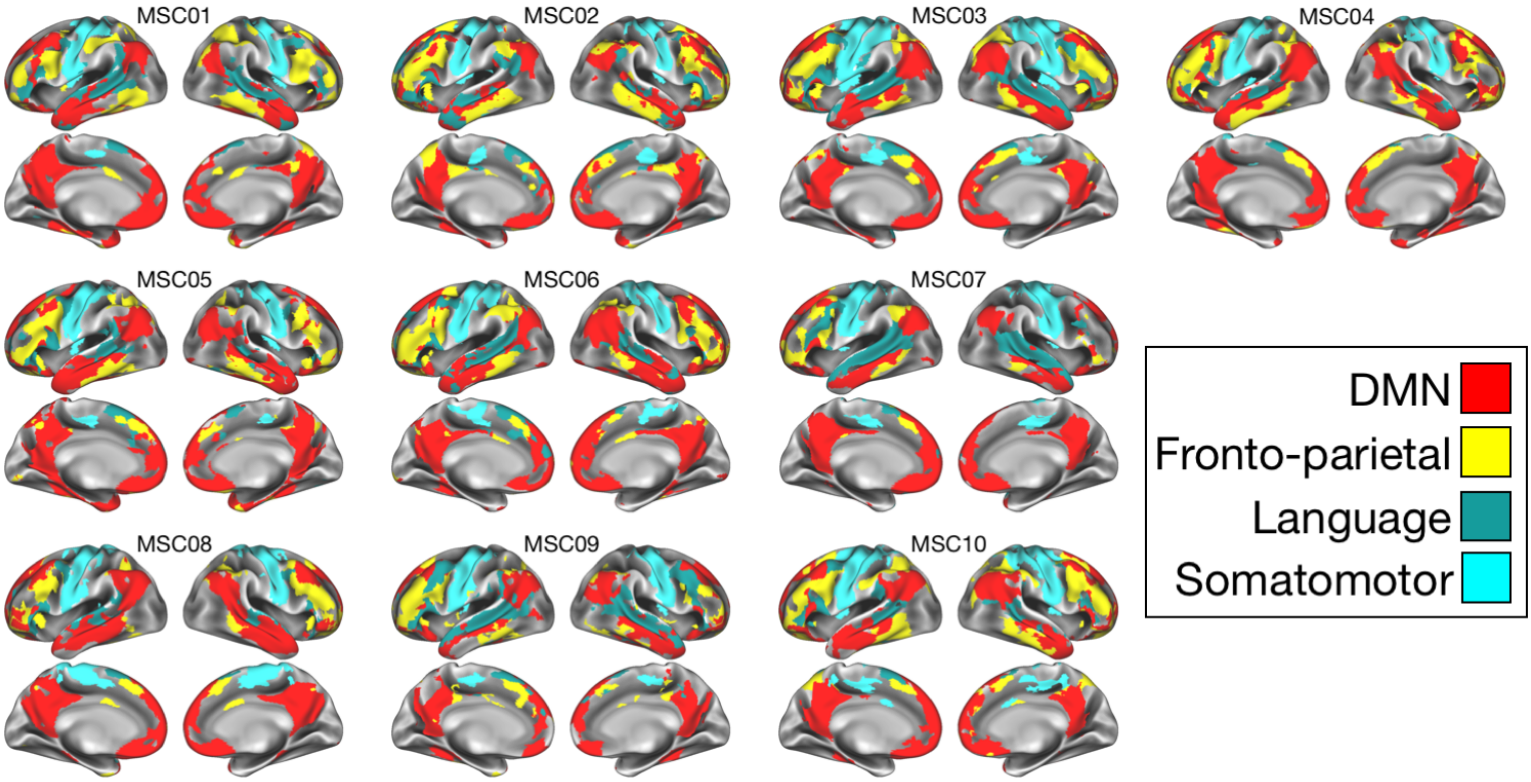

Figure S5: Large-scale networks in all subjects. Four relevant large-scale brain networks defined at high density in each subject. While most networks were identified at the 5% density level, in some subjects the Language network only separated from DMN at the 2% density level.

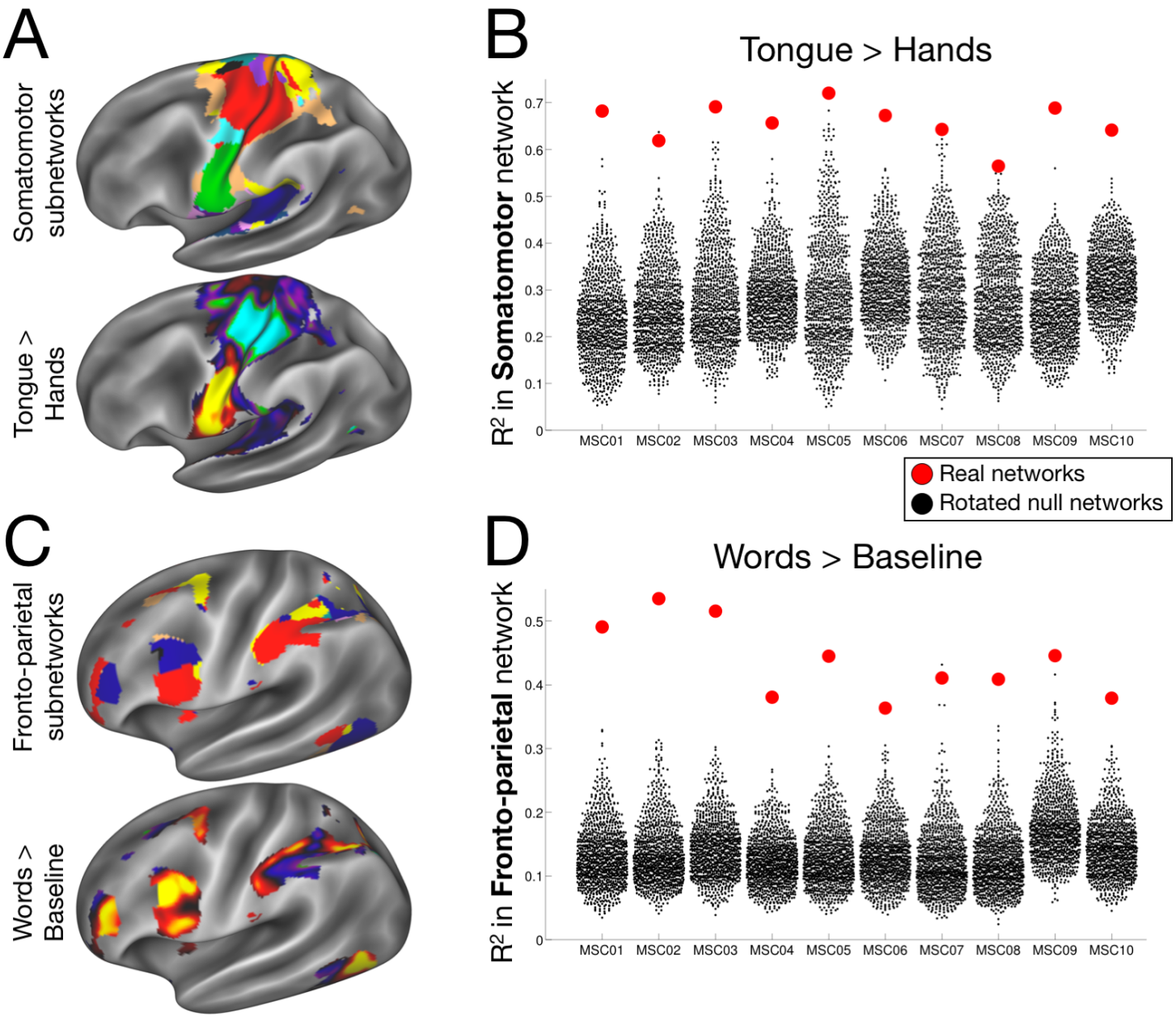

Figure S6: Subnetworks represent differentially task-activated divisions within the large-scale Somatomotor and Fronto-parietal networks. A,C) Task heterogeneity within the large-scale Somatomotor (A) and Fronto-parietal (C) networks in example subject MSC01. Subnetwork divisions (top) correspond very well with patterns of task activation (bottom) driven by Tongue > Hands (A) and Words > Baseline (C) contrasts. B,D) Variance in the pattern of Tongue > Hands (B) and Words > Baseline (D) task activation (y-axis) explained by Somatomotor (B) and Fronto-parietal (D) subnetwork divisions (red) and by rotated subnetworks (black), for each subject (x-axis).

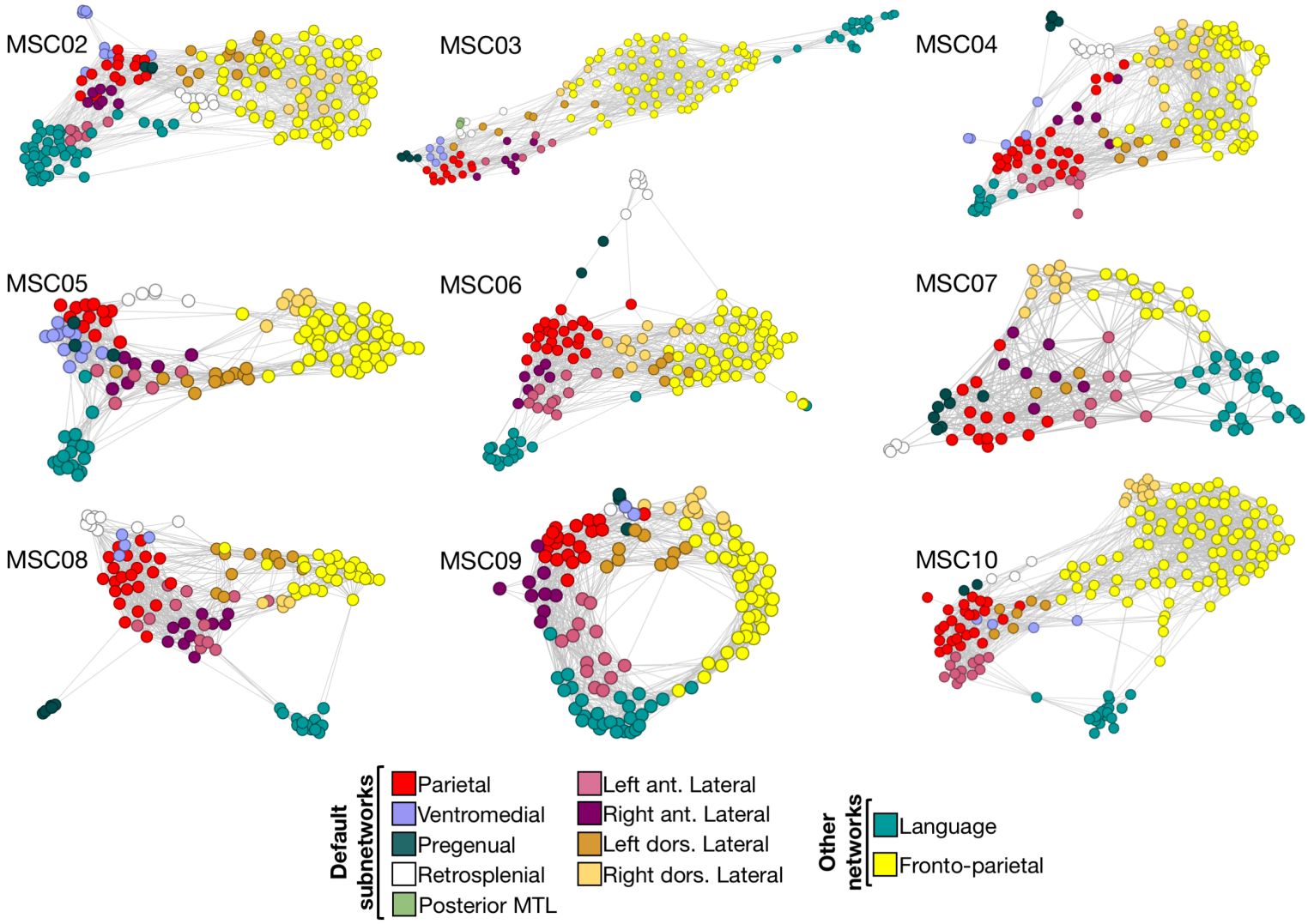

Figure S7: Spring-embedding plots illustrating relationships among DMN subnetworks and other networks in subjects MSC02-MSC10. Language and Fronto-parietal networks tend to be linked to specific DMN subnetworks.

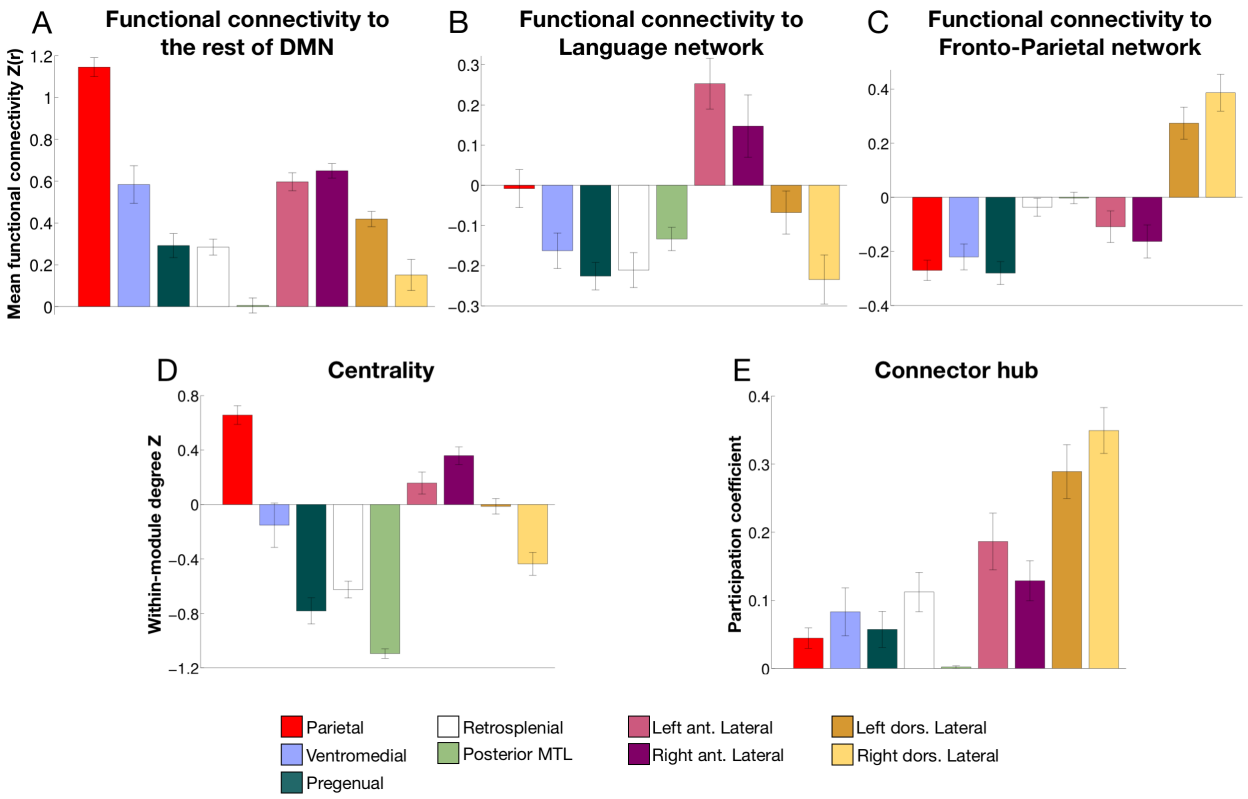

Figure S8: Functional connectivity strength to classic large-scale networks and network role across all DMN subnetworks. A) The Parietal subnetwork exhibited stronger functional connectivity to the rest of the DMN than any other subnetwork. B) The Anterior Lateral subnetworks both exhibited stronger connectivity to the Language network than any other subnetwork. C) The Dorsal Lateral subnetworks both exhibited stronger connectivity to the Fronto-parietal network than any other subnetwork. D) The Parietal subnetwork exhibited larger within-module degree Z-scores than any other subnetwork. E) The Lateral subnetworks exhibited numerically larger participation coefficients than any other subnetwork, though statistical comparisons between anterior Lateral and Ventromedial / Retrosplenial subnetworks were not significant.

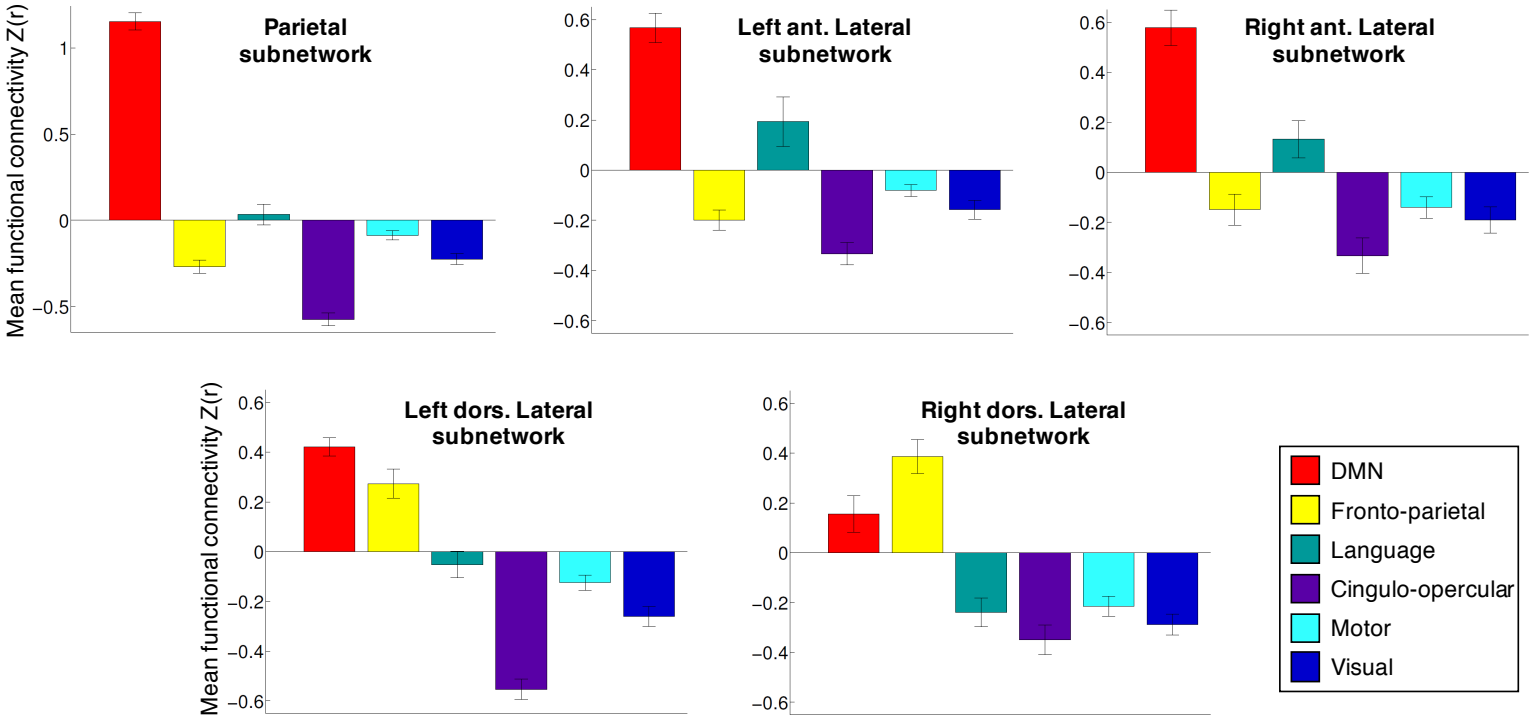

Figure S9: Mean functional connectivity between Default subnetworks and each large-scale network, identified at the 5% density level.

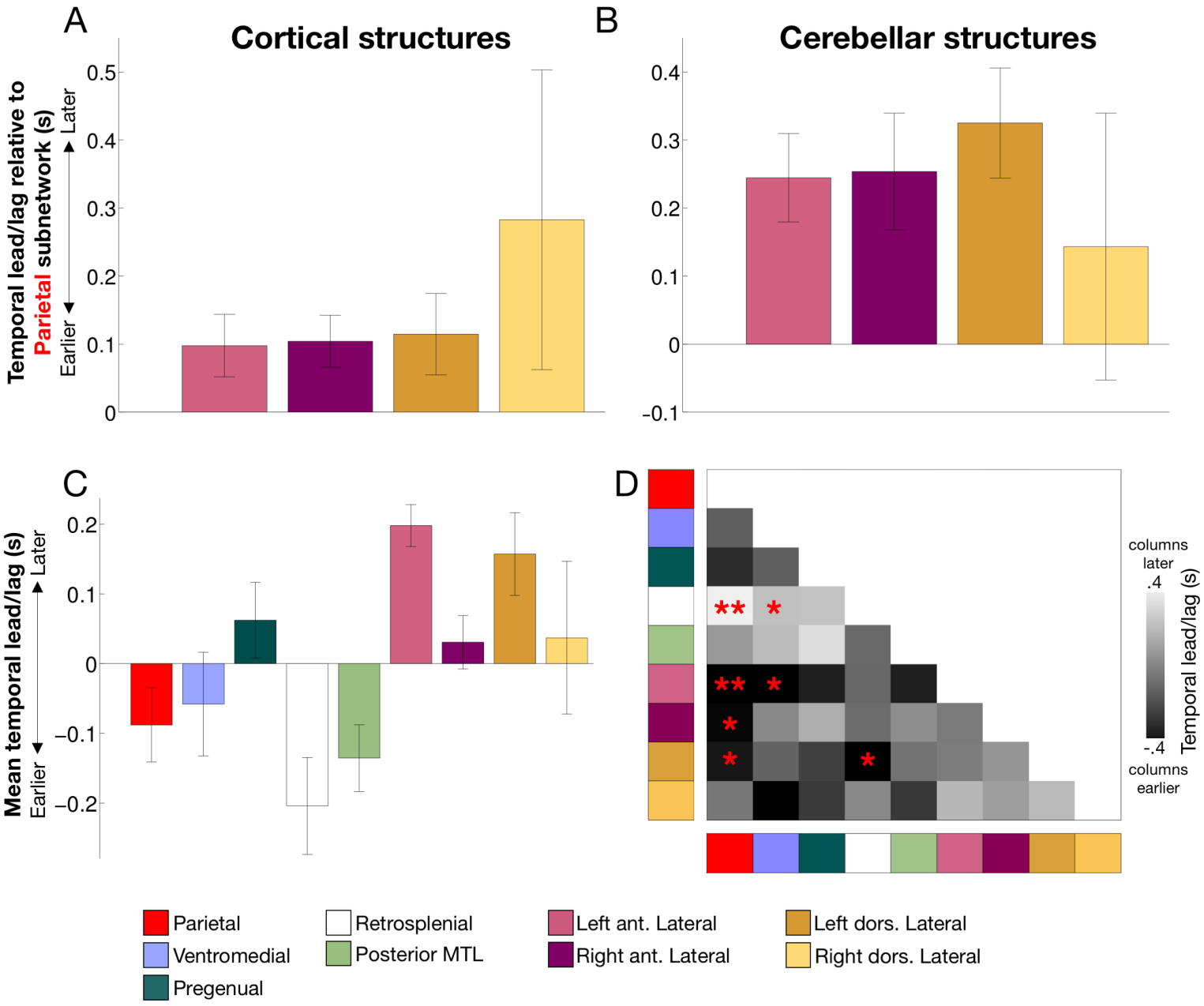

Figure S10: A,B): Three Lateral subnetworks lag the Parietal subnetwork within cortex and cerebellum. A) For cortical elements of subnetworks only, average lag of each Lateral subnetwork relative to the Parietal subnetwork. B) For cerebellar elements of subnetworks only, average lag of each Lateral subnetwork relative to the Parietal subnetwork. Positive values indicate Lateral signals are later than Parietal signals. C,D): Temporal relationships across all DMN subnetworks. C) Average temporal ordering of signals in each subnetwork relative to other subnetworks. D) Time-delay matrix indicating relative lead/lag of each network pairing. Dark cells indicate the "column" subnetwork is earlier; bright cells indicate the "row" subnetwork is earlier. ** p<.05 corrected ; * p<.05 uncorrected. Error bars show standard errors across subjects.

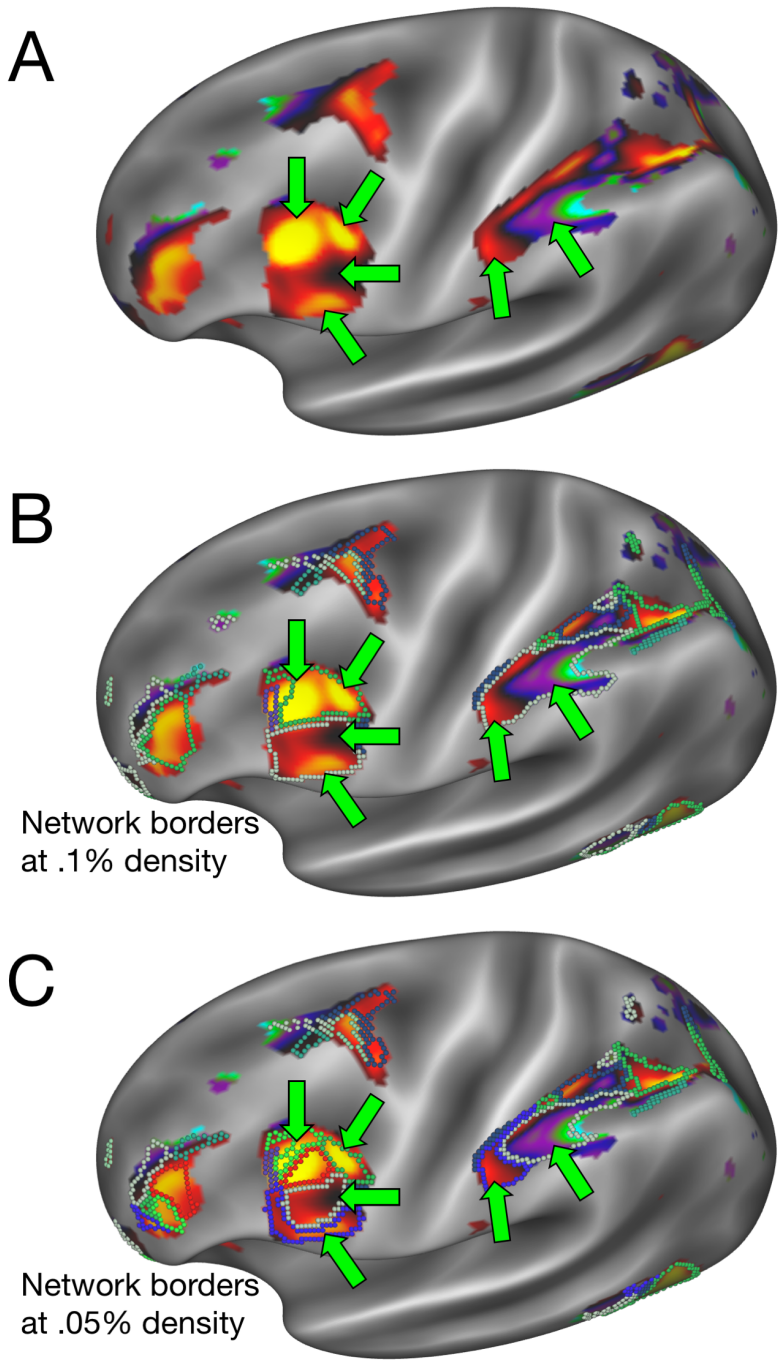

Figure S11: Subnetworks sparser than .1% may explain some additional variance in task activation. A) The Words > baseline contrast in subject MSC01, masked within the large-scale Fronto-parietal network (as defined at 5% density). Extensive activation heterogeneity is evident within this network. B) The same activation map, with subnetwork borders delineated at 1% density superimposed on top. These subnetworks explain much of the spatial variance within the Fronto-parietal network (as in Figure 2D). However, some subnetwork regions still exhibit heterogeneous activation (green arrows). C) The same activation map, with subnetwork borders delineated at .05% density superimposed on top. Much of the observed within-subnetwork heterogeneity in task activation in B) is now explained by the finer subnetwork divisions delineated at this density threshold.

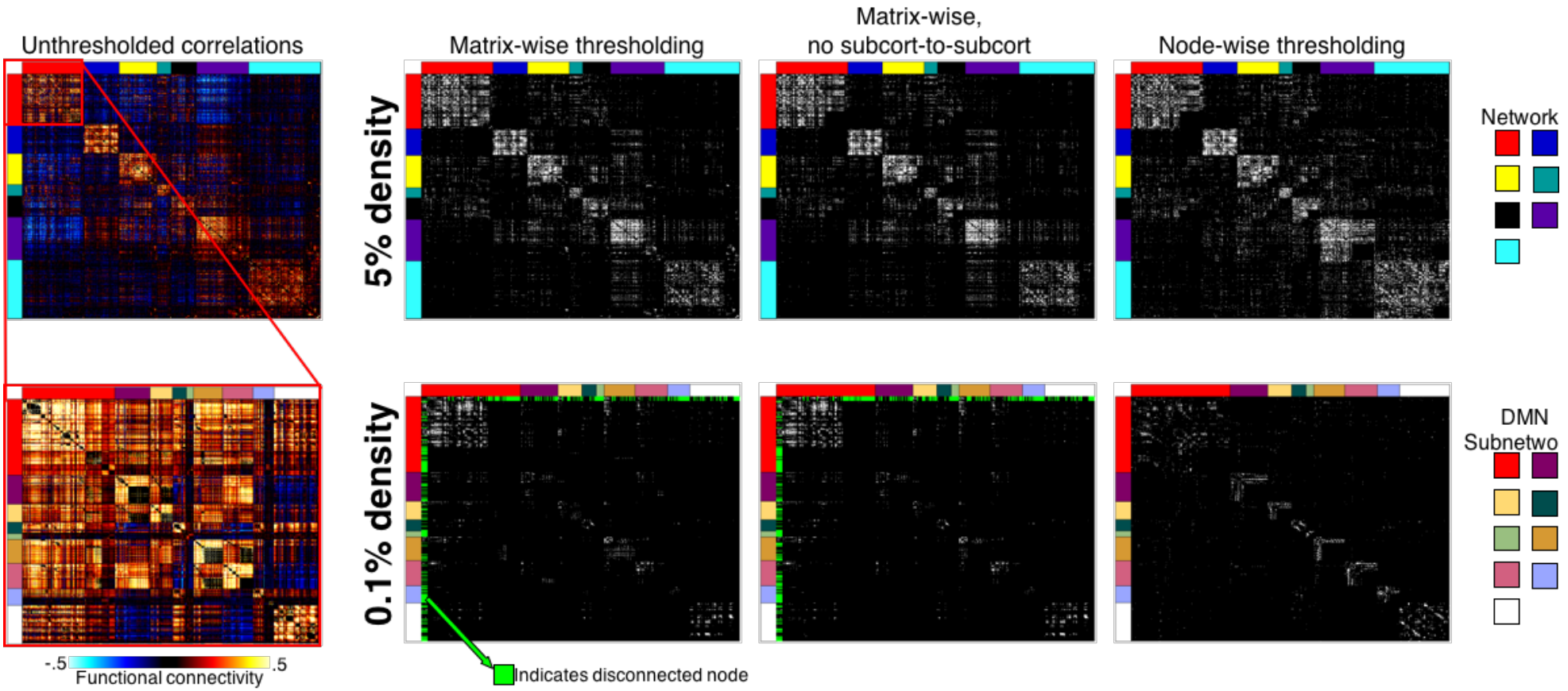

Figure S12: Illustration of connectivity matrix transformations. The first column shows the original connectivity matrix. The second column shows the graph that results from thresholding the connectivity matrix at a specific graph-wide density. The third column shows how this graph is altered by the removal of subcortical-to-subcortical connections. The last column shows how the graph is altered by applying node-specific thresholding, rather than graph-wide thresholding. The top row represents the whole-brain matrices thresholded at 5% (for display purposes, 10% of all vertices/voxels, randomly sampled, are shown here). The bottom row represents the matrices only within the Default network, thresholded at .1% (with no subsampling). Rows and columns are sorted by identified large-scale networks (top row) and Default subnetworks (bottom row). Green markings adjacent to the row and column axes indicate vertices/voxels that have no connections to any other vertex/voxel after thresholding. Note that the node-wise thresholding preserves and, in many cases, strengthens the block-wise structure, but also allows the matrix to be fully connected.

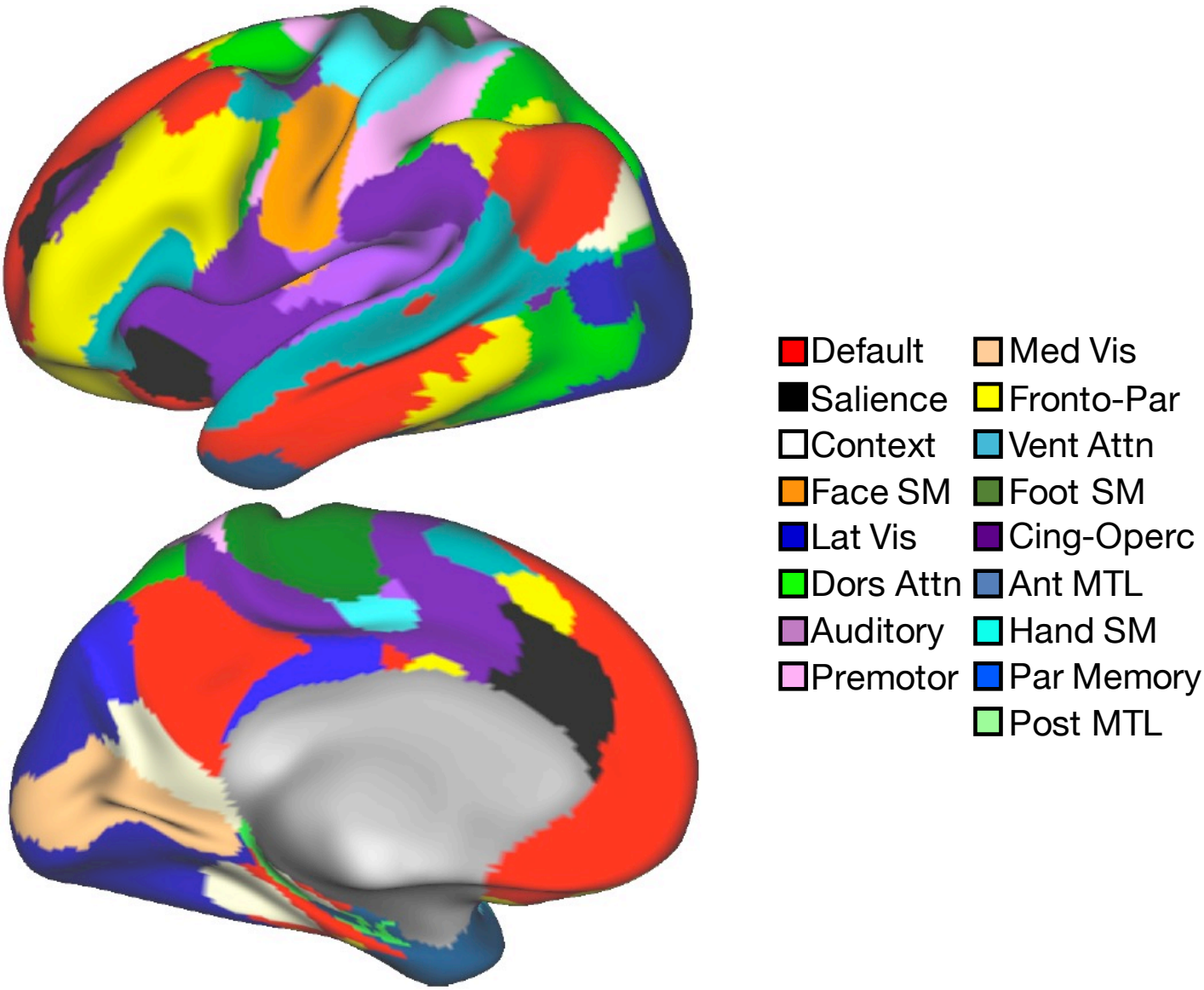

Figure S13: Independent group-level networks used for identification of individual-specific large-scale networks.

SI References

1. D. M. Barch, G. C. Burgess, M. P. Harms, S. E. Petersen, B. L. Schlaggar, M. Corbetta, M. F. Glasser, S. Curtiss, S. Dixit, C. Feldt, D. Nolan, E. Bryant, T. Hartley, O. Footer, J. M. Bjork, R. Poldrack, S. Smith, H. Johansen-Berg, A. Z. Snyder, D. C. Van Essen, Function in the human connectome: Task-fMRI and individual differences in behavior. *NeuroImage* **80**, 169–189 (2013).
2. J. W. Dubis, J. S. Siegel, M. Neta, K. M. Visscher, S. E. Petersen, Tasks Driven by Perceptual Information Do Not Recruit Sustained BOLD Activity in Cingulo-Opercular Regions. *Cereb. Cortex* **26**, 192–201 (2016).
3. L. Glass, Moiré effect from random dots. *Nature* **223**, 578–580 (1969).
4. S. Marek, J. S. Siegel, E. M. Gordon, R. V. Raut, C. Gratton, D. J. Newbold, M. Ortega, T. O. Laumann, B. Adeyemo, D. B. Miller, A. Zheng, K. C. Lopez, J. J. Berg, R. S. Coalson, A. L. Nguyen, D. Dierker, A. N. Van, C. R. Hoyt, K. B. McDermott, S. A. Norris, J. S. Shimony, A. Z. Snyder, S. M. Nelson, D. M. Barch, B. L. Schlaggar, M. E. Raichle, S. E. Petersen, D. J. Greene, N. U. F. Dosenbach, Spatial and Temporal Organization of the Individual Human Cerebellum. *Neuron* **100**, 977–993 (2018).
5. A. M. Dale, B. Fischl, M. I. Sereno, Cortical Surface-Based Analysis: I. Segmentation and Surface Reconstruction. *NeuroImage* **9**, 179–194 (1999).
6. B. Fischl, M. I. Sereno, A. M. Dale, Cortical Surface-Based Analysis: II: Inflation, Flattening, and a Surface-Based Coordinate System. *NeuroImage* **9**, 195–207 (1999).
7. D. C. Van Essen, M. F. Glasser, D. L. Dierker, J. Harwell, T. Coalson, Parcellations and Hemispheric Asymmetries of Human Cerebral Cortex Analyzed on Surface-Based Atlases. *Cereb. Cortex* **22**, 2241–2262 (2012).
8. E. C. Robinson, S. Jbabdi, M. F. Glasser, J. Andersson, G. C. Burgess, M. P. Harms, S. M. Smith, D. C. Van Essen, M. Jenkinson, MSM: a new flexible framework for Multimodal Surface Matching. *Neuroimage* **100**, 414–426 (2014).
9. M. F. Glasser, S. M. Smith, D. S. Marcus, J. L. R. Andersson, E. J. Auerbach, T. E. J. Behrens, T. S. Coalson, M. P. Harms, M. Jenkinson, S. Moeller, E. C. Robinson, S. N. Sotiropoulos, J. Xu, E. Yacoub, K. Ugurbil, D. C. Van Essen, The Human Connectome Project's neuroimaging approach. *Nat Neurosci* **19**, 1175–1187 (2016).
10. J. Talairach, P. Tournoux, *Co-planar stereotaxic atlas of the human brain* (Thieme Medical Publishers, Inc, 1988).
11. S. M. Smith, M. Jenkinson, M. W. Woolrich, C. F. Beckmann, T. E. J. Behrens, H. Johansen-Berg, P. R. Bannister, M. De Luca, I. Drobnjak, D. E. Flitney, R. K. Niazy, J. Saunders, J. Vickers, Y. Zhang, N. De Stefano, J. M. Brady, P. M. Matthews, Advances in functional and structural MR image analysis and implementation as FSL. *NeuroImage* **23**, S208–S219 (2004).
12. T. O. Laumann, E. M. Gordon, B. Adeyemo, A. Z. Snyder, S. J. Joo, M.-Y. Chen, A. W. Gilmore, K. B. McDermott, S. M. Nelson, N. U. F. Dosenbach, B. L. Schlaggar, J. A. Mumford, R. A. Poldrack, S. E. Petersen, Functional System and Areal Organization of a Highly Sampled Individual Human Brain. *Neuron* **87**, 657–670 (2015).
13. R. Ciric, D. H. Wolf, J. D. Power, D. R. Roalf, G. Baum, K. Ruparel, R. T. Shinohara, M. A. Elliott, S. B. Eickhoff, C. Davatzikos, R. C. Gur, R. E. Gur, D. S. Bassett, T. D. Satterthwaite, Benchmarking of participant-level confound regression strategies for the control of motion artifact in studies of functional connectivity. *Neuroimage* **154**, 174–187 (2017).

14. J. D. Power, B. L. Schlaggar, S. E. Petersen, Studying Brain Organization via Spontaneous fMRI Signal. *Neuron* **84**, 681–696 (2014).
15. C. Gratton, R. S. Coalson, A. Dworetsky, B. Adeyemo, T. O. Laumann, G. S. Wig, T. S. Kong, G. Gratton, M. Fabiani, D. M. Barch, D. Tranel, O. Miranda-Dominguez, D. A. Fair, N. U. F. Dosenbach, A. Z. Snyder, J. S. Perlmutter, S. E. Petersen, M. C. Campbell, Removal of high frequency contamination from motion estimates in single-band fMRI saves data without biasing functional connectivity. *bioRxiv*, 837161 (2019).
16. M. N. Hallquist, K. Hwang, B. Luna, The nuisance of nuisance regression: Spectral misspecification in a common approach to resting-state fMRI preprocessing reintroduces noise and obscures functional connectivity. *Neuroimage* **82**, 208–225 (2013).
17. J. Carp, Optimizing the order of operations for movement scrubbing: Comment on Power et al. *NeuroImage* **76**, 436–438 (2013).
18. J. D. Power, B. L. Schlaggar, S. E. Petersen, Recent progress and outstanding issues in motion correction in resting state fMRI. *NeuroImage* **105**, 536–551 (2015).
19. B. Fischl, FreeSurfer. *NeuroImage* **62**, 774–781 (2012).
20. R. Patriat, E. K. Molloy, R. M. Birn, Using Edge Voxel Information to Improve Motion Regression for rs-fMRI Connectivity Studies. *Brain Connect* **5**, 582–595 (2015).
21. T. D. Satterthwaite, M. A. Elliott, R. T. Gerraty, K. Ruparel, J. Loughead, M. E. Calkins, S. B. Eickhoff, H. Hakonarson, R. C. Gur, R. E. Gur, D. H. Wolf, An improved framework for confound regression and filtering for control of motion artifact in the preprocessing of resting-state functional connectivity data. *Neuroimage* **64**, 240–256 (2013).
22. Y. Behzadi, K. Restom, J. Liau, T. T. Liu, A component based noise correction method (CompCor) for BOLD and perfusion based fMRI. *NeuroImage* **37**, 90–101 (2007).
23. M. F. Glasser, S. N. Sotiropoulos, J. A. Wilson, T. S. Coalson, B. Fischl, J. L. Andersson, J. Xu, S. Jbabdi, M. Webster, J. R. Polimeni, D. C. Van Essen, M. Jenkinson, WU-Minn HCP Consortium, The minimal preprocessing pipelines for the Human Connectome Project. *Neuroimage* **80**, 105–124 (2013).
24. D. Marcus, J. Harwell, T. Olsen, M. Hodge, M. Glasser, F. Prior, M. Jenkinson, T. Laumann, S. Curtiss, D. Van Essen, Informatics and Data Mining Tools and Strategies for the Human Connectome Project. *Front. Neuroinform.* **5**, 4 (2011).
25. F. M. Miezin, L. Maccotta, J. M. Ollinger, S. E. Petersen, R. L. Buckner, Characterizing the hemodynamic response: effects of presentation rate, sampling procedure, and the possibility of ordering brain activity based on relative timing. *Neuroimage* **11**, 735–759 (2000).
26. J. M. Ollinger, M. Corbetta, G. L. Shulman, Separating Processes within a Trial in Event-Related Functional MRI: II. Analysis. *NeuroImage* **13**, 218–229 (2001).
27. R. L. Buckner, F. M. Krienen, A. Castellanos, J. C. Diaz, B. T. T. Yeo, The organization of the human cerebellum estimated by intrinsic functional connectivity. *J. Neurophysiol.* **106**, 2322–2345 (2011).
28. D. J. Greene, S. Marek, E. M. Gordon, J. S. Siegel, C. Gratton, T. O. Laumann, A. W. Gilmore, J. J. Berg, A. L. Nguyen, D. Dierker, A. N. Van, M. Ortega, D. J. Newbold, J. M. Hampton, A. N. Nielsen, K. B. McDermott, J. L. Roland, S. A. Norris, S. M. Nelson, A. Z. Snyder, B. L. Schlaggar, S. E. Petersen, N. U. F. Dosenbach, Integrative and Network-Specific Connectivity of the Basal Ganglia and Thalamus Defined in Individuals. *Neuron* **105**, 742–758 (2020).